Article

Discovery Medicine 2026; 38(209): 1908–1926
https://doi.org/10.24976/Discov.Med.202638209.149

Multi-Omics Research Combined With Experimental Verification to Identify Potential Targets for Temporomandibular Joint Osteoarthritis

Xibei Li[1,2,3], Xingyu Li[1,2,3], Shaoyang Yu[1,2,3], Chenzhi Li[4], Yingyue Zhang[1,2,3], Wenke Yang[1,2,3], Haoting Wu[1,2,3], Jun Guo[1,2,3], Xueyao Jiang[1], Qiang Zhang[1,2,3], Xiao Yan[1,2,3], Xiao Yuan[1,2,3,*]

[1]Department of Orthodontics, The Affiliated Hospital of Qingdao University, 266003 Qingdao, Shandong, China
[2]School of Stomatology, Qingdao University, 266023 Qingdao, Shandong, China
[3]Department of Central Laboratory, The Affiliated Hospital of Qingdao University, 266003 Qingdao, Shandong, China
[4]Department of Orthodontics, Affiliated Stomatological Hospital of Nanjing Medical University, 210029 Nanjing, Jiangsu, China
*Correspondence: yuanxiaoqd@qdu.edu.cn (Xiao Yuan)
Submitted: 6 February 2026 Revised: 19 April 2026 Accepted: 29 April 2026 Published: 20 June 2026

Background: Temporomandibular joint osteoarthritis (TMJ OA) is a degenerative joint disease characterized by cartilage destruction and subchondral bone remodeling. However, its molecular mechanisms remain incompletely understood, and effective therapeutic targets are still limited. This study aimed to identify candidate targets for TMJ OA through an integrated multi-omics strategy combined with experimental validation.

Methods: Multi-layer omics data including expression quantitative trait loci (eQTL), protein quantitative trait loci (pQTL) and molecular quantitative trait loci (mQTL) were merged with TMJ OA Genome-Wide Association Study (GWAS) summary stats. Mendelian Randomization (MR) and colocalization analyses were performed to determine whether there was a causal relationship between the genes. The main results were further validated by immune infiltration analysis, pathway enrichment (Gene Set Enrichment Analysis, GSEA), transcription factor and miRNA network analysis, drug prediction (Connectivity Map, CMap), and molecular docking. A rat forced mandibular retrusion (FMR) model was used for *in vivo* experimental validation.

Results: haloacid dehalogenase like hydrolase domain containing 3 (*HDHD3*) and high mobility group 20B (*HMG20B*) were prioritized as candidate genes associated with TMJ OA. Colocalization analysis supported shared signals between TMJ OA and the pQTLs of *HDHD3* and *HMG20B*. Transcriptomic validation showed that *HDHD3* was significantly upregulated in the diseased group ($p < 0.05$). Pathway analyses suggested that *HDHD3* was associated with glycolysis- and lactylation-related alterations. In the animal model, mechanical stress significantly increased *HDHD3* expression and lactylation-related signals ($p < 0.05$) and was accompanied by cartilage and subchondral bone damage. Folic acid was identified as a candidate compound through drug prediction and molecular docking.

Conclusion: This study provides multi-omics and experimental evidence suggesting that *HDHD3* and *HMG20B* are candidate genes associated with TMJ OA. Notably, *HDHD3* may be involved in glycolysis- and lactylation-related alterations during TMJ OA progression. Folic acid was identified as a candidate compound, but its therapeutic relevance requires further validation.

Keywords: temporomandibular joint osteoarthritis; multi-omics; lactylation; glycolysis; folic acid

Introduction

The temporomandibular joint (TMJ) is a key paired joint that connects the jaw to the skull, enabling essential functions like facial movement, eating, and speaking [1]. Temporomandibular joint osteoarthritis (TMJ OA) is a common and complex disorder of this joint. Its main symptoms include joint pain, clicking sounds, abnormal jaw movement, and in severe cases, facial deformity, which causes significant physical and emotional distress and reduces quality of life [2]. TMJ OA involves inflammation of the joint lining, cartilage damage, and changes in the underlying bone. Common treatments range from non-surgical options like counseling, physical therapy, bite splints, and medication to surgery [3]. However, current treatment options often fall short, and due to a lack of understanding of the disease's onset and progression, clinicians are currently unable to prevent it or effectively relieve patients' symptoms.

Advancements in bioinformatics have changed how we look into TMJ OA's molecular roots [4]. In recent years, population genetics has emerged as a valuable tool for drug discovery and development, showing great potential in identifying and verifying possible therapeutic tar-

gets [5]. With the fast development of high-throughput technologies, tens of thousands of Quantitative Trait Locis (QTLs) can now be readily visualized [6,7], providing important information for biomarker identification and drug development. Mendelian Randomization (MR) is a genetic causal inference approach that strengthens the credibility of these bioinformatics findings [8,9], and provides important information about causality from such data [10]. Based on Mendel's laws of inheritance, this method uses Single Nucleotide Polymorphisms (SNPs) as Instrumental Variables (IVs) to effectively deduce the causal relationship between controlled risk exposure factors and medical outcomes [11,12]. This study, by integrating Genome-Wide Association Study (GWAS) and molecular QTL data (such as gene expression QTL, protein abundance QTL, and methylation modified QTL) aimed to perform causal inference using MR, and thoroughly search for possible target genes for TMJ OA from three perspectives: methylation modification, gene expression, and protein abundance [13].

The purpose of this study was to integrate multi-omics and genetic evidence to identify candidate genes associated with TMJ OA and to explore a potential metabolic-epigenetic mechanism centered on HDHD3.

Materials and Methods

This study integrated TMJ OA GWAS summary statistics with multiple molecular QTL datasets, including expression quantitative trait loci (eQTL), protein quantitative trait loci (pQTL), and molecular quantitative trait loci (mQTL), to identify and prioritize candidate genes associated with TMJ OA. Briefly, molecular QTL instruments were harmonized with the FinnGen R12 TEMPOROMANDIB GWAS dataset and analyzed using Mendelian randomization across the three omics layers. Candidate genes identified from the MR analyses were further prioritized by overlap analysis, colocalization analysis, and reverse MR analysis (Fig. 1). The prioritized genes were subsequently evaluated through transcriptomic validation, immune infiltration analysis, pathway enrichment, regulatory network construction, drug prediction, molecular docking, and experimental validation in a rat forced mandibular retrusion model.

Data Download

(1) Transcriptomic data: Gene expression profiles (GSE289871) were acquired from the GEO database (https://www.ncbi.nlm.nih.gov/geo/), which consists of 14 samples (7 control groups/7 disease groups), with the platform annotation being GPL24014.

(2) Exposure data: eQTL: From eQTLGen Consortium (Phase II; https://www.eqtlgen.org) for blood-based genome-wide meta-analyses. mQTL: Used EUR cohort meta-analysis data (n = 3701 European-ancestry whole-blood samples; 426,636 traits) from PMID: 38548728 [14]. pQTL: From deCODE (2021 release; https://www.decode.com/summarydata/), which includes GWAS (https://www.finngen.fi/en/access_results) of 35,559 Europeans with 4907 plasma protein aptamers [15].

(3) Phenotypic data: FinnGen database (https://r12.risteys.finngen.fi/) gave case-control stats on temporomandibular disorders (finngen_R12_TEMPOROMANDIB: 7966 cases vs. 262,404 controls).

Mendelian Randomization Analysis of mQTL, eQTL and pQTL

IVs were selected from exposure-associated SNPs in the QTL summary statistics using a significance threshold of $p < 1 \times 10^{-5}$. Linkage disequilibrium clumping was then performed with an R^2 threshold of <0.001 and a window size of 10,000 kb to ensure the independence of the selected variants. SNPs associated with secondary phenotypes ($p < 5 \times 10^{-5}$) were excluded, and weak instruments were removed using an F-statistic threshold of <10. After harmonization of effect alleles between the exposure and outcome datasets, MR analyses were performed to evaluate the associations between molecular traits and TMJ OA. The inverse-variance weighted (IVW) method was used as the primary analytical approach, while MR-Egger, weighted median, weighted mode, and Wald ratio were applied as complementary methods to assess the robustness of the findings under different assumptions regarding IV validity. In this study, IVW $p < 0.05$ was used as the initial screening threshold for candidate associations. Candidate genes identified at this stage were subsequently subjected to further prioritization analyses.

The initial discovery-stage screening criterion used the IVW $p < 0.05$ threshold to identify candidate associations across multiple omics layers. Given the broad screening framework, these associations were not interpreted as definitive evidence on their own. Instead, candidate genes were further prioritized through cross-omics comparison, colocalization analysis, reverse MR, transcriptomic support, and experimental observations. To improve robustness assessment for the prioritized genes, we systematically compared effect estimates across complementary MR methods, including IVW, MR-Egger, weighted median, and weighted mode, and further performed heterogeneity testing, MR-Egger intercept analysis, MR-PRESSO global testing, and leave-one-out sensitivity analysis where applicable.

Sensitivity Analysis and Heterogeneity Analysis

To evaluate the robustness of the MR results, sensitivity analyses were performed, including leave-one-out analysis and heterogeneity testing. Leave-one-out analysis was used to determine whether the observed association was disproportionately driven by any single SNP. Heterogeneity among IVs was assessed to evaluate the consistency of

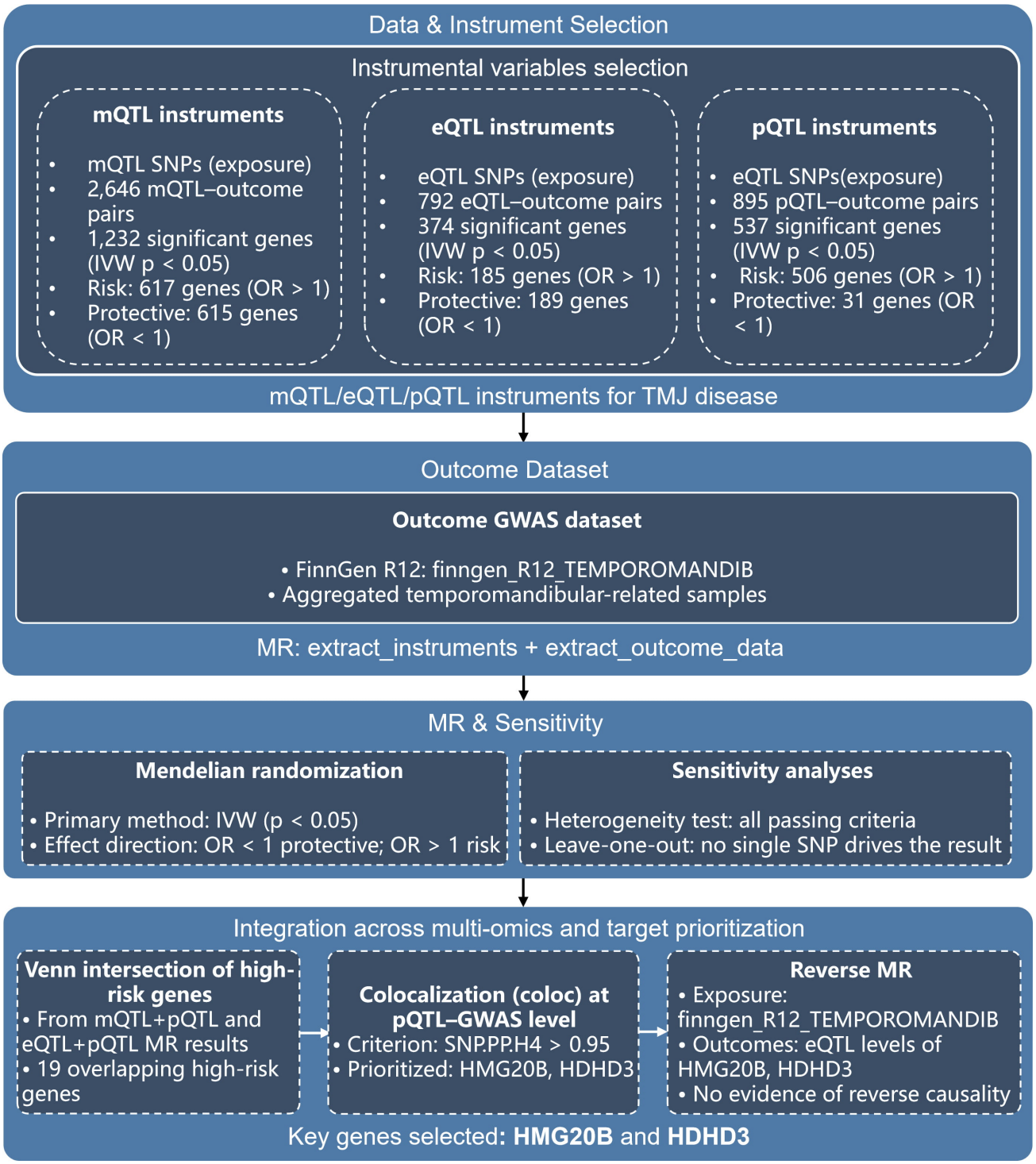

Fig. 1. Technical workflow for selecting key candidate genes. eQTL, expression quantitative trait loci; pQTL, protein quantitative trait loci; mQTL, molecular quantitative trait loci; SNPs, Single Nucleotide Polymorphisms; IVW, inverse-variance weighted; OR, odds ratio; GWAS, Genome-Wide Association Study; TMJ, Temporomandibular joint; MR, Mendelian Randomization; HDHD3, haloacid dehalogenase like hydrolase domain containing 3; HMG20B, high mobility group 20B.

causal estimates across SNPs. In addition, candidate associations were further examined by colocalization analysis and reverse MR analysis to support the prioritization of key genes.

Co-Localization Analysis

We performed colocalization analysis using the coloc method to evaluate whether the pQTL signal and the TMJ OA GWAS signal shared a common causal variant. Variants within a 100-kb region centered on the index SNP were

extracted for analysis. Posterior probabilities were calculated for the coloc hypotheses, and a posterior probability for hypothesis 4 (PP.H4) >0.95 was considered evidence supporting a shared causal variant between the pQTL and GWAS signals.

Immune Infiltration

Immune infiltration analysis was performed using the deconvo_xcell() function in the IOBR package. Given that xCell was originally developed mainly for complex immune- and tumor-related transcriptomic contexts, and considering the relatively small sample size, complex tissue composition, and uncertain tissue origin of the TMJ OA dataset analyzed in this study, the xCell-based results were treated as exploratory analyses. Therefore, these inferred infiltration scores were used primarily for descriptive comparison and preliminary correlation analyses, rather than as stand-alone evidence for mechanistic interpretation.

GSEA Analysis

The patients were separated into high and low expression groups based on some specific key genes. Genes were grouped according to the Gene Set Enrichment Analysis (GSEA) that used MSigDB's (https://www.gsea-msigdb.org/gsea/msigdb) version 7.0 annotated gene sets as a reference frame for genome-wide pathway comparison among all groups. The pathways' differential expression between different groups were compared. Significantly enriched gene sets (adjusted p-value < 0.05) were ranked according to their consistency scores. GSEA analysis is usually applied to explore the connection between disease classification and biological significance.

GSVA Analysis

Gene Set Variation Analysis (GSVA) transforms a gene-level expression matrix into pathway enrichment scores. We used gene sets from MSigDB and applied GSVA to evaluate various pathway perturbations across different samples. Because this method does not require predefined sample groups, it can detect subtle biological changes across diverse sample groups.

Transcription Factor Regulatory Network

This study applied RcisTarget package for predicting transcription factors (TFs) with DNA sequence motifs serving as the computational basis. The NES value of motifs was adjusted based on the total amount of motifs contained within the reference database. Other motifs were identified through similarity analysis and gene orthology assessments in addition to the initial annotations. For each motif-gene set pair, the AUC was computed using recovery curves of genes ranked by binding affinity. The final NES values came from the AUC distribution among all motifs within targeted gene groups.

Key Gene-Related Non-Coding RNA Networks

MicroRNAs (miRNAs)—small non-coding RNAs that control gene expression by degrading mRNA or repressing translation—found within significant genes influencing pathogenic gene transcription or stability were studied. Key gene-related miRNAs were retrieved from the miRCode database (https://bio.tools/miRcode) and then displayed using Cytoscape software (version 3.10.1; Cytoscape Consortium, San Diego, CA, USA).

CMap Drug Prediction

The CMap database (https://clue.io/) from the Broad Institute was used, which contains transcriptional profiles of 1309 bioactive compounds across five human cell lines at various doses and time points. Functional connections among compounds, genes, and diseases were then identified, and disease-specific DEGs were used to predict potential therapeutic agents.

Molecular Docking

The corresponding three-dimensional protein structures of the key genes were obtained from the AlphaFold database (https://alphafold.com/). Drug prediction for these genes was then performed using the CTD database (https://www.ctdbase.org/) to obtain relevant information. The molecular structures of the compounds were accessed via the PubChem database (https://pubchem.ncbi.nlm.nih.gov/). AutoDock software (version 1.5.7; The Scripps Research Institute, La Jolla, CA, USA). was used for molecular docking, and the genetic algorithm was run 50 times. The results with the lowest binding energies were selected and imported into PyMOL (version 2.4; Schrödinger, LLC, New York, NY, USA) for visualization, highlighting the binding sites of small molecules on proteins.

Animal Model Establishment

The animal model utilized the previously developed and published forced mandibular retrusion (FMR) technique [16]. Twenty-four male Sprague-Dawley rats aged six weeks and of SPF grade were purchased from Beijing Vital River Laboratory Animal Technology Co., Ltd. (Beijing, China; License No. SCXK (Beijing) 2021-0006). The rats were randomly divided into the control group, 2-week experimental group, and 4-week experimental group, with 8 rats in each group. Histological evaluation, imaging assessment, and image-based quantitative analysis were performed in a blinded manner whenever applicable. The sample size was determined based on preliminary experimental experience. The experimental cohort underwent sustained mandibular retraction force application via personalized stainless steel intermaxillary devices to induce atypical mechanical stress on the TMJ. Intervention durations were 2 and 4 weeks. Rats in the experimental groups were anesthetized by intraperitoneal injection of 1% sodium pen-

tobarbital at a dose of 0.35 mL/100 g body weight before the experimental procedure. Control subjects did not undergo any intervention. At the end of the experiment, rats were euthanized by intraperitoneal injection of 5% sodium pentobarbital at a dose of 0.4 mL/100 g body weight, equivalent to 200 mg/kg. Procedures were performed by trained personnel in accordance with the approved institutional animal care and use protocol and standard operating procedures. Animals were monitored until a stable state of unconsciousness was achieved and death was confirmed using institutionally approved criteria. The temporomandibular joints were then harvested for subsequent analyses.

Micro-CT Analysis

Micro computed tomography (Micro-CT), an X-ray imaging method that visualizes bone at a resolution of 1–100 µm, allows precise measurements of the internal bone microstructure. scanning was performed using a Bruker SkyScan 1276 micro-CT scanner (Bruker, Kontich, Belgium).

Histologic and Immunohistochemical Assessment

The collected fresh tissue samples were fixed in 4% paraformaldehyde solution (Cat. No. P1110; Beijing Solarbio Science & Technology Co., Ltd., Beijing, China) for 24 h, decalcified for 4 days using formic acid decalcification solution (Cat. No. G2490; Beijing Solarbio Science & Technology Co., Ltd., Beijing, China), embedded in paraffin, and cut into 6 µm-thick sections.

For hematoxylin and eosin (H&E) staining, paraffin sections were baked in a 60 °C oven for approximately 60 min, deparaffinized in xylene I and xylene II (Cat. No. 10023418; Sinopharm Chemical Reagent Co., Ltd., Shanghai, China) for 15 min each, rehydrated through a graded ethanol series using absolute ethanol (Cat. No. 100092683; Sinopharm Chemical Reagent Co., Ltd., Shanghai, China), and rinsed in distilled water. The sections were then stained with a hematoxylin and eosin staining kit (Cat. No. G1120; Beijing Solarbio Science & Technology Co., Ltd., Beijing, China) for 3–5 min, differentiated in hydrochloric acid alcohol differentiation solution (Cat. No. BA4025C; Zhuhai Beso Biotechnology Co., Ltd., Zhuhai, China) for 15 s, blued in ammonia water bluing solution (Zhuhai Beso Biotechnology Co., Ltd., Zhuhai, China) for 30–60 s, and counterstained with eosin for 5 min. After dehydration and clearing, the sections were mounted with neutral resin (Cat. No. 10004160; Sinopharm Chemical Reagent Co., Ltd., Shanghai, China). For Safranin O-fast green staining, paraffin sections were routinely deparaffinized to water and stained using a Safranin O-fast green staining kit (Cat. No. G1371; Beijing Solarbio Science & Technology Co., Ltd., Beijing, China) , with fast green staining for 5 min, differentiation in freshly prepared 1% acetic acid alcohol for 30 s, and Safranin O staining for 5 min. After dehydration, clearing, and mounting, the Safranin O-fast green-stained sections were scanned using a Pannoramic MIDI slide scanner (3DHISTECH Ltd., Budapest, Hungary), and the digital images were used to evaluate cartilage matrix changes and proteoglycan loss.

For immunohistochemical staining, after blocking and antigen retrieval, the sections were incubated overnight at 4 °C with primary antibodies against L-lactyl lysine (Cat. No. PTM-1401RM; rabbit monoclonal antibody; PTM Biolabs, Hangzhou, China; diluted 1:100 in PBS) and HDHD3 (Cat. No. HY-P89143; mouse monoclonal IgG2a antibody; MedChemExpress, Monmouth Junction, NJ, USA; diluted 1:150 in PBS). The sections were then incubated at room temperature for 60 min with species-matched secondary antibodies, including Goat Anti-rabbit secondary antibody (Cat. No. E-AB-1003; Elabscience Biotechnology Co., Ltd., Wuhan, China; diluted 1:1000) for the rabbit primary antibody and Goat Anti-mouse secondary antibody (Cat. No. E-AB-1001; Elabscience Biotechnology Co., Ltd., Wuhan, China; diluted 1:1000) for the mouse primary antibody. Signals were subsequently visualized using DAB and counterstained with hematoxylin.

The above stained sections were scanned with Pannoramic MIDI scanner ((3DHISTECH Ltd., Budapest, Hungary) to capture images. Immunohistochemical results were quantified using Fiji software bundled with ImageJ 1.54p (National Institutes of Health, Bethesda, MD, USA).
RNA Extraction and RT-qPCR

Rat cartilage tissue was scraped off and cut into small pieces using blades, then immediately frozen in liquid nitrogen and ground into powder. Total RNA was isolated as per the manufacturer's instructions. After reverse transcription of cDNA according to the kit's instructions, quantitative real-time PCR was performed using ChamQ Universal SYBR qPCR Master Mix (Cat. No. Q711; Vazyme Biotech Co., Ltd., Nanjing, China) on a LightCycler 96 Real-Time PCR System (Roche, Basel, Switzerland). The primer sequences used for RT-qPCR analysis are listed in Table 1.

Statistical Analysis

R software (version 4.1.0; R Foundation for Statistical Computing, Vienna, Austria) and public databases were used for statistical analysis. All data are given as mean ± SD. Student's *t*-test was performed for comparison between two groups. Graphs were drawn using GraphPad Prism (version 10.0; GraphPad Software, Boston, MA, USA). $|\log FC| > 2$ and p-value < 0.05 were considered significant, and $p < 0.01$ extremely significant.

Results

eQTL Mendelian Randomization Analysis

Result identifier was set to finngen_R12_TEMPOROMANDIB, which is based on the combined statistics of the temporomandibular joint-related samples. To determine if there is a cause-and-effect

Table 1. Primer sequences used for RT-qPCR analysis.

Primers	Sequence (5′ → 3′)
ARID3B-F	GCTGTTTGCCCAGAAACCAG
ARID3B-R	TTGGTGAGCAGTGAGAGCTG
AHNAK-F	GAGGTGATGCAGAACTCCCC
AHNAK-R	CAAGCCAACAGTGTGATGCC
HMG20B-F	TTCTGGGCTCATGAACACCC
HMG20B-R	TCTTCCGTGAAGATGGGCAC
HDHD3-F	GTCGGGGAGGAATATGCCAG
HDHD3-R	TCAGTGAGAGATGCTGTACC
IL-1β-F	GCCAACAAGTGGTATTCTCC
IL-1β-R	CTTTCATCACACAGGACAGG
GAPDH-F	AACCCATCACCATCTTCCAGG
GAPDH-R	GCCTTCTCCATGGTGGTGAA

The data were analysed using the comparative cycle threshold method, and the relative expression levels were determined by the $2^{-\Delta\Delta CT}$ measurement with reference to GAPDH.

RT-qPCR, reverse transcription quantitative polymerase chain reaction; ARID3B, AT-rich interaction domain 3B; F, forward primer; R, reverse primer; AHNAK, AHNAK nucleoprotein; HMG20B, high mobility group 20B; HDHD3, haloacid dehalogenase like hydrolase domain containing 3; IL-1β, interleukin-1β; GAPDH, glyceraldehyde-3-phosphate dehydrogenase.

link between 792 sets of eQTLs and the outcome, the extract_instruments and extract_outcome_data tools were used. Also, 374 causative relationships with positive eQTL outcomes were found using MR analysis (IVW *p*val < 0.05). Results showed that 189 genes were associated with a lower risk of temporomandibular joint disorders (OR <1), whereas 185 genes were associated with a higher risk (OR >1) in the eQTL-based MR analysis (Fig. 2A). We then examined the causal relationships of these 374 genes to determine whether they were stable and reliable. Additional validation analyses were conducted for the selected gene pairs. A heterogeneity test on the 374 genes showed that all of them met the required conditions. In addition, the leave-one-out analysis revealed that no single SNP had a significant impact on the overall error range when removed; therefore, the 374 pairs were considered stable.

pQTL Mendelian Randomization Analysis

pQTL protein data were obtained from the deCODE database. To assess potential causal relationships between pQTLs and the outcome, we used extract_instruments and extract_outcome_data, yielding 895 pairs for further analysis (table.OR.txt). Also, 537 pairs of PQTL-related genes were chosen using MR for causality testing (IVW *p*val < 0.05). In the pQTL-based MR analysis, 31 genes were associated with a lower risk of temporomandibular joint disorders (OR <1), whereas 506 genes were associated with a higher risk (OR >1) (Fig. 2B). We then assessed the stability of these causal associations by examining heterogeneity across 537 potentially relevant genetic loci, all of which passed the required tests. In order to test the reliability of these causal inferences, we performed a leave-one-out sensitivity analysis on the 537 genetic pairs, evaluating the influence of each individual SNP on the overall estimate by excluding one SNP at a time. The results showed that removing any single SNP did not lead to significant changes in the overall error line, indicating that the 537 identified causal pairs were relatively stable.

mQTL Mendelian Randomization Analysis

To find out the cause-and-effect relationship between 2646 pairs of MQTLS and their outcomes, we extracted the instrument and outcome information. Also, the causality of 1232 positive outcomes of MQTL-related genes were screened by MR analysis (IVW *p*val < 0.05). In the mQTL-based MR analysis, 615 genes were associated with a lower risk of temporomandibular joint disorders (OR <1), whereas 617 genes were associated with a higher risk (OR >1) (Fig. 2C). Then we tested 1232 genes for heterogeneity and all genes passed the heterogeneity test.

We further performed sensitivity analysis on these 1232 MQTL-related genes to assess the reliability of the results. The results showed that removing any one SNP from the SNP set did not substantially change the overall estimate, suggesting that the 1232 SNPs selected for causal inference were reliable.

Co-Localization Analysis and Reverse MR Analysis

To identify the most relevant genes associated with temporomandibular joint disorders, we intersected the high-risk genes identified from the eQTL, pQTL, and mQTL MR analyses and obtained 19 overlapping genes (Fig. 3A). These genes were then subjected to colocalization analysis at the pQTL-GWAS level. The results showed that HDHD3 and HMG20B displayed strong evidence of colocalization with TMJ OA, with PP.H4 values greater than 0.95, suggesting that the pQTL and disease association signals may be driven by shared causal variants (Fig. 3B,C). Reverse MR analysis further showed that temporomandibular joint disorders did not have a significant causal effect on the expression-related traits of HDHD3 and HMG20B (Fig. 3D). Together, these findings supported the prioritization of HDHD3 and HMG20B for subsequent analyses. In our transcriptome analysis, in order to provide supportive transcriptomic evidence, we further examined the expression patterns of the genetically implicated genes in the GEO dataset. Although the transcriptomic cohort was relatively limited in size, HDHD3 was significantly upregulated in the diseased group compared with the control group ($p < 0.05$), whereas the difference in HMG20B expression was not statistically significant ($p > 0.05$) (Fig. 3E).

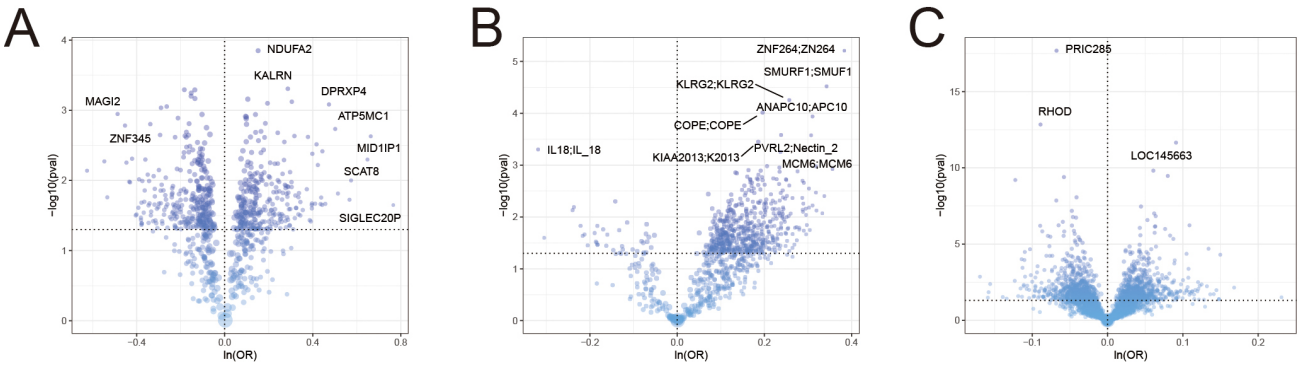

Fig. 2. eQTL-, pQTL-, and mQTL-based MR. (A) eQTL-MR: distributions of ORs and *p* values across tested associations. (B) pQTL-MR: distributions of ORs and *p* values across tested associations. (C) mQTL-MR: distributions of ORs and *p* values across tested association. In each panel, each point represents one gene. Genes located on the right side of the x-axis ($x > 0$) were defined as higher-risk genes, whereas genes on the left side ($x < 0$) were considered lower-risk or protective genes. Genes above the horizontal dashed line represent significant associations with $p < 0.05$.

To further assess the robustness of the prioritized genes, we compared effect estimates across complementary MR methods and performed sensitivity analyses. At the pQTL layer, HDHD3 showed significant positive associations in the IVW, weighted median, and weighted mode analyses, whereas HMG20B showed positive associations in the IVW and MR-Egger analyses, with directionally consistent estimates in the other methods. No significant directional pleiotropy was detected based on MR-Egger intercept testing, and MR-PRESSO global testing was not statistically significant for both prioritized genes. Leave-one-out analyses suggested that the observed associations were not driven by any single SNP. Detailed MR estimates and sensitivity analyses for the prioritized genes are provided in **Supplementary Tables 1,2** and **Supplementary Figs. 1,2**.

Differential Expression and Immune Infiltration of Key Genes in the Transcriptome

To explore potential differences in the immune-related transcriptomic landscape between control and disease samples, we performed an xCell-based deconvolution analysis (Fig. 4A,B). Given the methodological constraints of applying xCell to a small and heterogeneous TMJ OA dataset, the results were interpreted as preliminary descriptive findings. More specifically, compared with the control group, the disease group showed significant differences in several inferred immune or stromal cell subsets, including increased Adipocytes_xCell, CD8+_Tcm_xCell, CMP_xCell, Mast_cells_xCell, Plasma_cells_xCell, and Smooth_muscle_xCell, as well as decreased Basophils_xCell and MSC_xCell ($p < 0.05$, Fig. 4C). Correlation analysis further showed that HMG20B was significantly negatively correlated with CD8+_naive_T-cells_xCell, CD8+_T-cells_xCell, CD8+_Tem_xCell, and Macrophages_M2_xCell ($p < 0.05$), whereas HDHD3 was significantly positively correlated with Plasma_cells_xCell and Smooth_muscle_xCell ($p < 0.05$) (Fig. 4D). In addition, we explored the relationships between the prioritized genes and multiple immune-related components, including chemokines, receptors, MHC-related genes, immunoinhibitors, and immunostimulators (Fig. 5A–E). These observations should be regarded as exploratory findings rather than stand-alone mechanistic evidence.

Signaling Pathways Involved in Key Genes

Next, we explored the specific signaling pathways associated with the key genes and investigated the molecular mechanisms by which these genes influence disease development. According to the GSEA results, HMG20B was enriched in the B cell receptor signaling pathway, Toll-like receptor signaling pathway, Notch signaling pathway, and other pathways (Fig. 6A,C). HDHD3 was enriched in the Hippo signaling pathway, MAPK signaling pathway, cAMP signaling pathway, among others (Fig. 6B,D). GSVA analysis showed that HDHD3 was enriched in GLYCOLYSIS, ESTROGEN_RESPONSE_LATE, and other signaling pathways (Fig. 6E). HMG20B is enriched in MITOTIC_SPINDLE and INTERFERON_ALPHA_RESPONSE signaling pathways (Fig. 6F). Some key genes may influence disease progression through these mechanisms.

Key Gene-Related Non-Coding RNA Networks and Transcription Factor Regulatory Networks

The research team then performed reverse prediction of key genes using the mircode database and identified 32 microRNAs, making up 40 mRNA-miRNA interaction pairs, and visualized the results in cytoscape (Fig. 7A). The analysis identified these major genetic components and showed that they were regulated by shared biological processes, particularly the coordinated activity of multiple transcription factors. Then, cumulative recovery curves

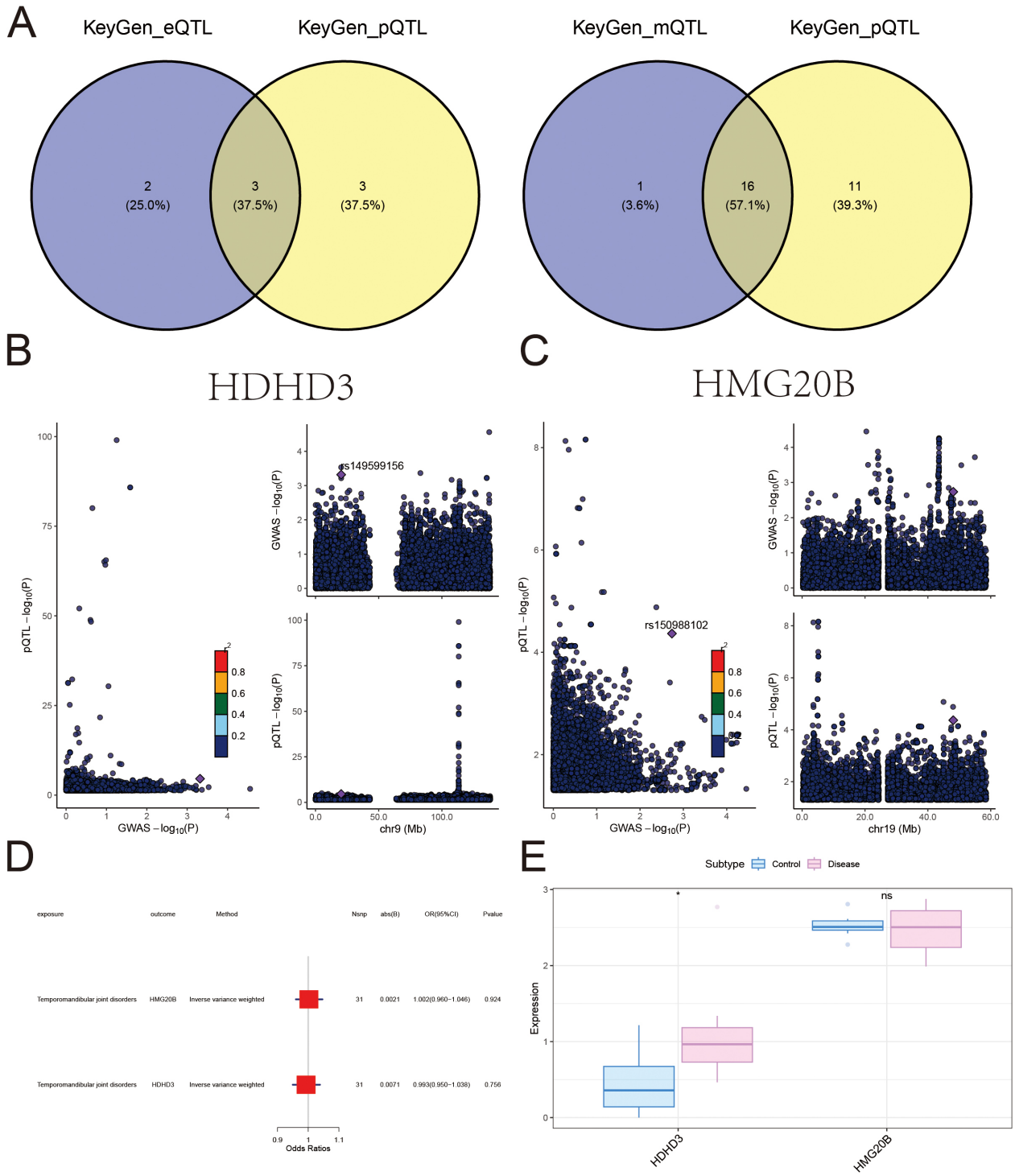

Fig. 3. Colocalization analysis, reverse MR, and expression validation of key genes. (A) Overlap analysis of up-regulated candidate genes across different omics layers. The left Venn diagram shows the intersection between up-regulated genes identified from the eQTL and pQTL analyses, whereas the right Venn diagram shows the intersection between up-regulated genes identified from the mQTL and pQTL analyses. (B) pQTL-GWAS colocalization analysis for HDHD3 (lead SNP: rs149599156). (C) pQTL-GWAS colocalization analysis for HMG20B (lead SNP: rs150988102). (D) Reverse Mendelian randomization analysis of the key genes HMG20B and HDHD3. (E) Relative expression levels of HDHD3 and HMG20B in the validation dataset. * indicates $p < 0.05$; ns indicates $p > 0.05$.

(Fig. 7B) indicated that these transcription factors were highly enriched. In the motif-tf annotation analysis of key genes, cisbp__M0148 motif had the highest standardized enrichment score of 7.99. We displayed all enriched motifs and their linked transcription factors for the key genes (Fig. 7C).

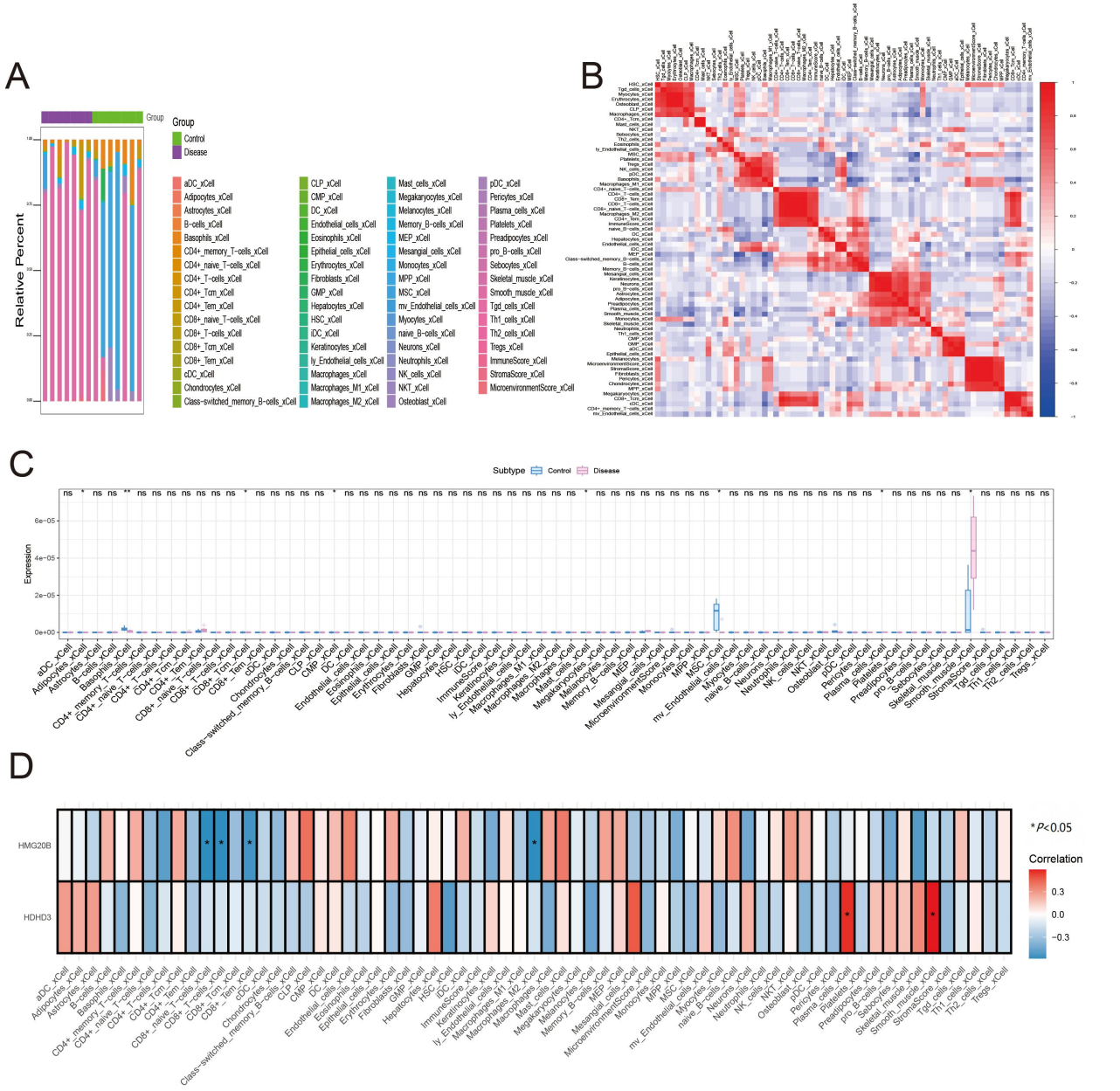

Fig. 4. Immune infiltration analysis. (A) Relative proportions of immune/cell subsets in control and disease samples. (B) Correlation heatmap of inferred infiltration levels among cell subsets (red, positive; blue, negative). (C) Comparison of inferred cell subset infiltration levels between the control and disease groups. * indicates $p < 0.05$; ** indicates $p < 0.01$; ns indicates $p > 0.05$. (D) Correlations between the expression of the key genes (HMG20B and HDHD3) and inferred cell subset infiltration levels. Colors indicate correlation coefficients; * indicates $p < 0.05$.

Relationship Between Key Genes and Lactylation-Related Genes

In a previous study entitled "Lactylation-Related Gene Signature Effectively Predicts Prognosis and Treatment Responsiveness in Hepatocellular Carcinoma" [17], the authors showed that lactylation-related genes were associated with disease progression and treatment responsiveness, highlighting the potential biological significance of lactylation-related signatures. Based on this, we further examined the expression patterns of lactylation-related genes in our transcriptomic dataset. Among the 20 lactylation-related genes analyzed, several showed differential expression between the two groups. In addition, correlation analysis between the key genes and lactylation-related genes demonstrated that HDHD3 was positively correlated with AHNAK (r = 0.850) and negatively correlated with ARID3B (r = –0.795) (Fig. 8A).

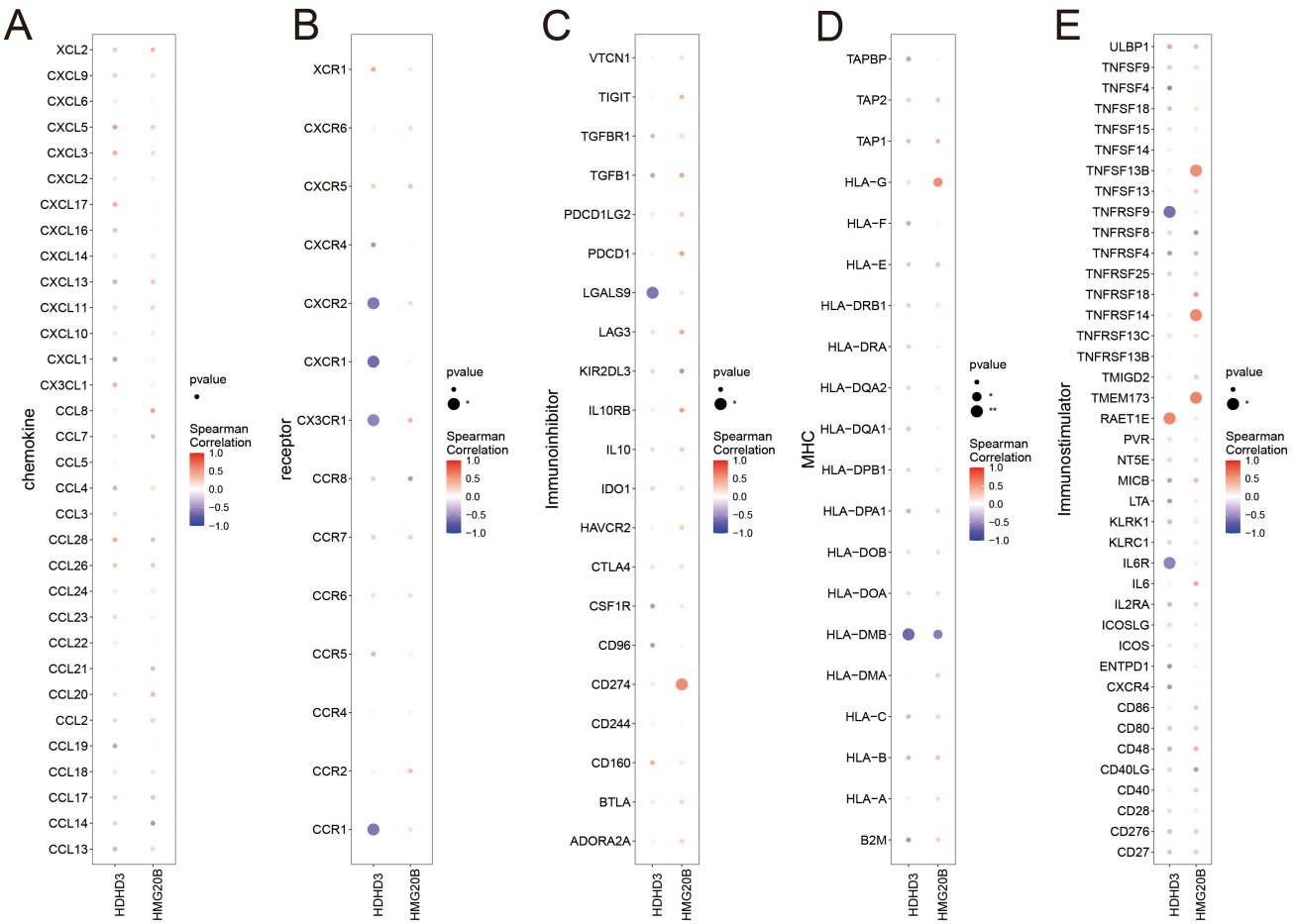

Fig. 5. Correlation between immune-related genes and cell subsets. (A) Correlation between chemokine-related genes and immune cell subsets: colors represent Spearman correlation coefficients, with *p* values indicated by dot size. (B) Correlation between receptor-related genes and immune cell subsets. (C) Correlation between MHC-related genes and immune cell subsets. (D) Correlation between Immunoinhibitor genes and immune cell subsets. (E) Correlation between Immunostimulator genes and immune cell subsets. In all panels, colors represent Spearman correlation coefficients, and dot size indicates p values. Statistical significance is indicated as * indicates $p < 0.05$; ** indicates $p < 0.01$. MHC, major histocompatibility complex.

CMap Drug Prediction

In this study, the limma package was used to perform differential gene expression analysis on expression data from the two patient groups. Screening criteria for differential genes included: $|\log FC| > 0.585$ and $p < 0.05$, a total of 1159 differential genes were screened out, including 743 up-regulated genes and 416 down-regulated genes. Then, volcano maps and heat maps were generated to visualize the differential expression results (Fig. 8B). We divided the top 150 down-regulated differentially expressed genes into two groups and used the Connectivity Map database to predict the drug targeting of differentially expressed genes. The results show that the expression patterns of drug disruptions such as linezolid, harpagoside, TG100-115, and PKCbeta-inhibitor have significant negative correlations with the expression patterns of disease disruptions, and drugs may alleviate or even reverse the disease state (Fig. 8C).

Molecular Docking Results

Proteins and compounds selected by key genes were HMG20B: Q9P0W2-Folic Acid and HDHD3: Q9BSH5-Folic Acid. Molecular docking results indicated that the binding energy of HMG20B: Q9P0W2-Folic Acid was –4.07 kcal/mol, while that of HDHD3: Q9BSH5-Folic Acid was –6.02 kcal/mol. The results showed that the binding energy between the protein and small molecule was low, suggesting a stable docking interaction (Fig. 9A–D).

In addition, an interaction network between the key genes and candidate molecules was constructed (Fig. 9E,F). In this network, each node represents a molecule, and the edges indicate the interactions or associations derived from molecular docking analysis. This visualization further illustrates the potential relationships between the prioritized target proteins and the candidate compounds [18,19].

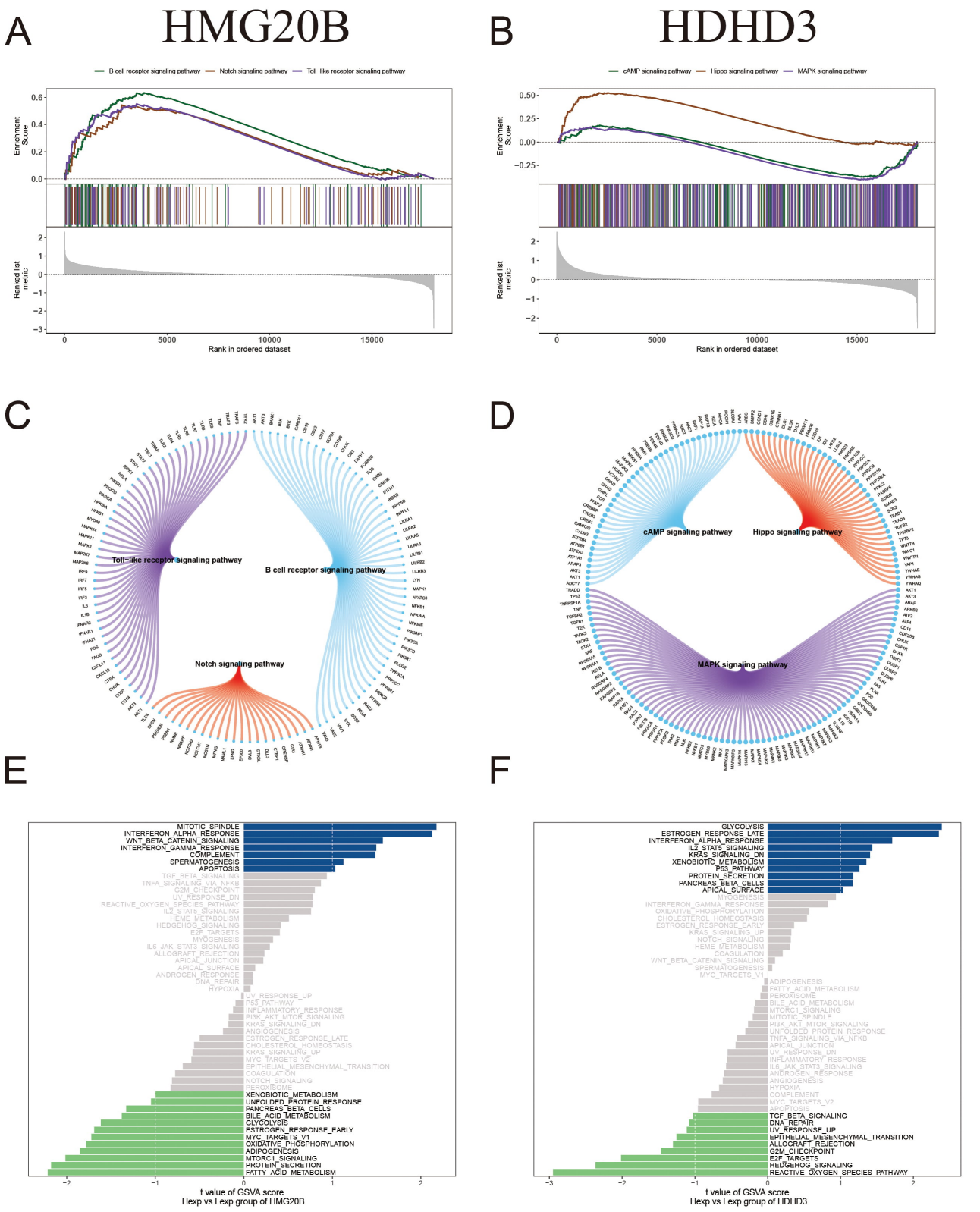

Fig. 6. KEGG pathway analysis and GSVA for key genes. (A,B) GSEA enrichment plots of KEGG pathways associated with HMG20B and HDHD3, respectively. (C,D) KEGG pathway-gene networks associated with HMG20B and HDHD3, respectively. (E,F) GSVA results for the key genes based on the Hallmark gene set; blue indicates pathways enriched in the high-expression group, and green indicates pathways enriched in the low-expression group. KEGG, Kyoto Encyclopedia of Genes and Genomes; GSEA, Gene Set Enrichment Analysis; GSVA, Gene Set Variation Analysis.

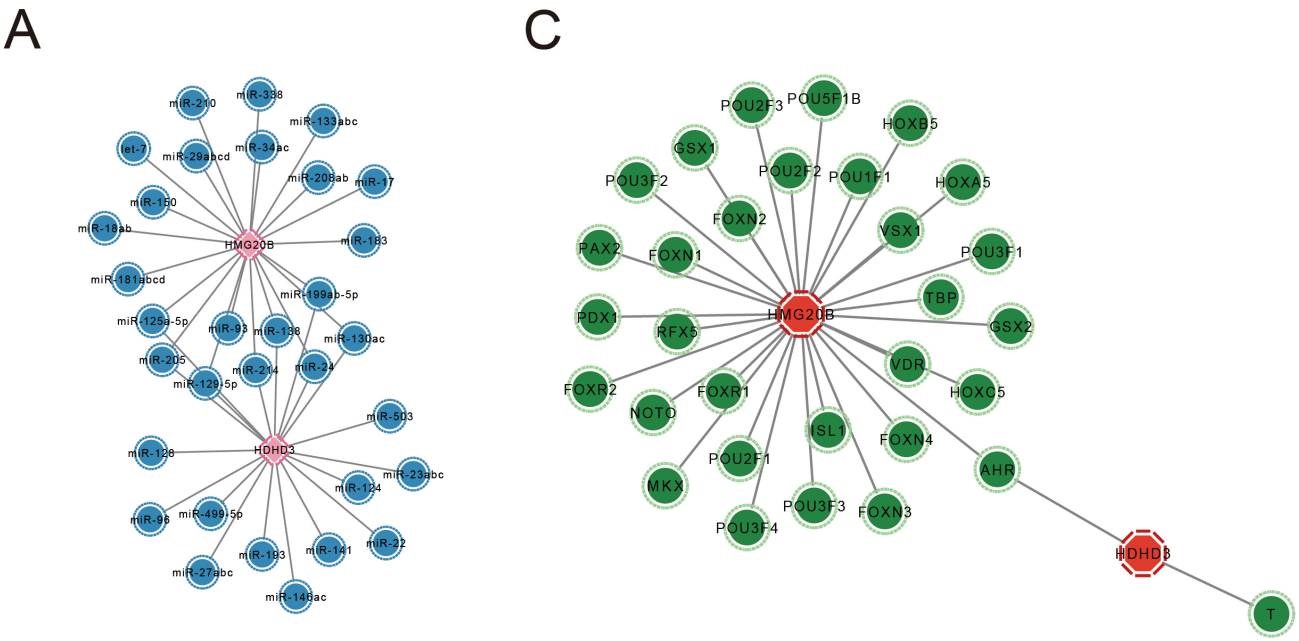

Show 5 entries Search:

	logo	geneSet	motif	NES	AUC	TF_highConf	nEnrGenes	enrichedGenes
	All	All	All	All	All	All	All	All
1		key_gene	cisbp__M0148	7.99	0.914		2	HDHD3;HMG20B
2		key_gene	cisbp__M1462	6.77	0.781		2	HDHD3;HMG20B
3		key_gene	cisbp__M4708	4.14	0.494	TBP (directAnnotation).	1	HMG20B
4		key_gene	cisbp__M1245	4.07	0.487		1	HMG20B
5		key_gene	cisbp__M4825	4.07	0.487		1	HMG20B

Showing 1 to 5 of 50 entries Previous 1 2 3 4 5 ⋯ 10 Next

Fig. 7. miRNA and transcriptional regulatory networks for key genes. (A) miRNA network for key genes: pink represents mRNA, blue represents miRNA. (B) Transcriptional regulatory network for key genes: red represents key genes, green represents transcription factors. (C) Display of all enriched motifs for key genes and their corresponding transcription factors.

In Vivo Validation Results

In H&E and safranin O-fast green sections (Fig. 10A,B), the field of view was focused on the posterior oblique sagittal section of the rat condyle. They showed great variation in condylar morphology and layering. In the control group, the continuous surface, intact tidemark, and uniform distribution of chondrocytes could be observed. The area of Safranin O staining was large and uniform. On the contrary, in the 2W and 4W groups, the cartilage layer seemed to be thinner with disordered, clustered or even vacuolated chondrocytes. They had damaged or drifting tidemark and thickened, calcified cartilage which invaded into the upper layer. The area of the safranin O staining was significantly reduced, and a large area of the section was replaced with fast green staining.

In addition, micro-CT scanning and 3D reconstruction of the condyles (Fig. 10C) showed that the control group exhibited a relatively intact cortical surface and compact subchondral bone structure, whereas the experimental groups showed obvious bone resorption and structural deterioration. Compared with the control group, the 2W group showed significantly decreased BV/TV, Tb.Th, Tb.N, BMD, and TMD and significantly increased Tb.Sp

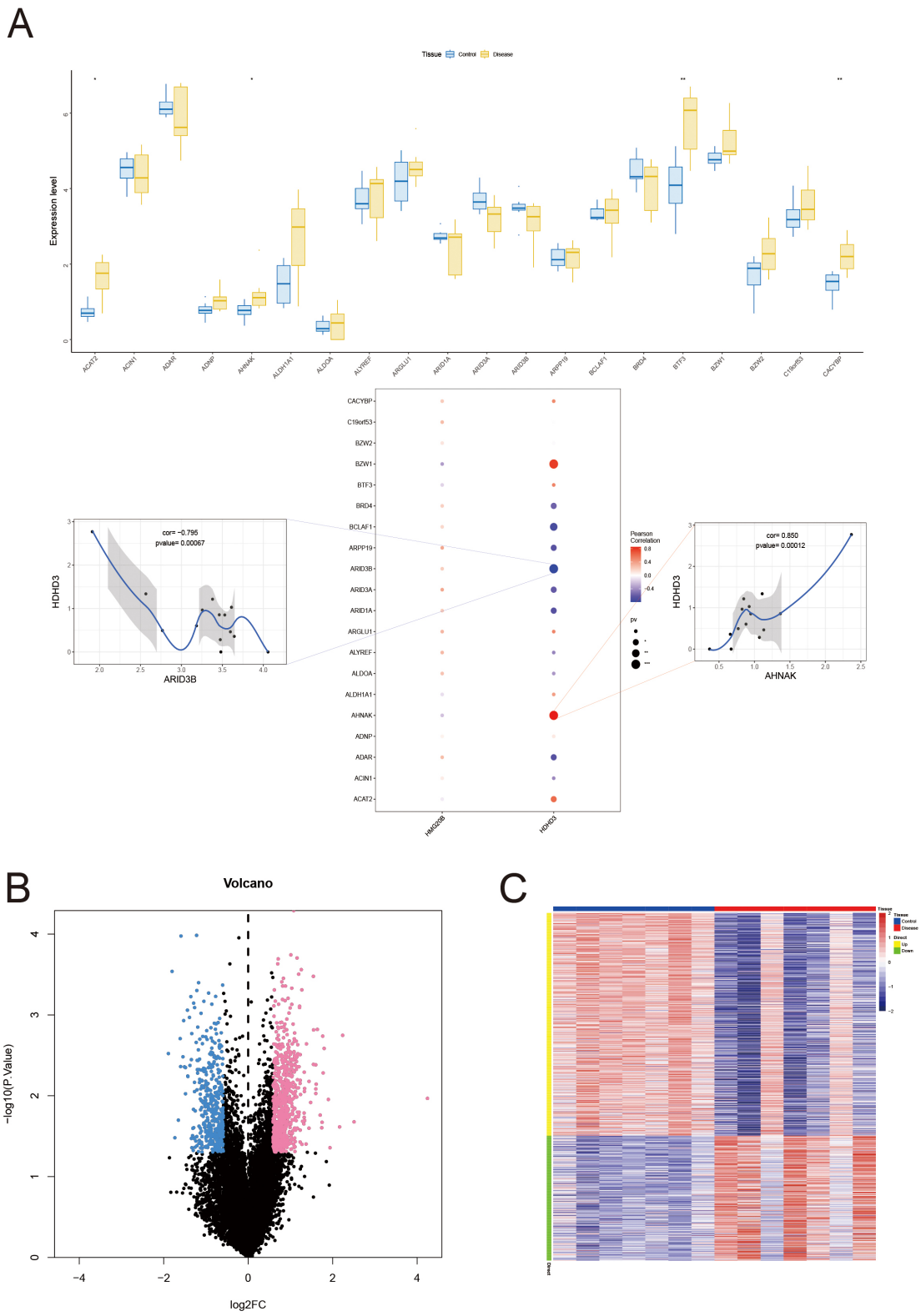

Fig. 8. Disease association and differential analysis. (A) Top: Differential expression of disease-related genes in control and disease samples. Bottom: Correlation analysis between HDHD3 and disease-related genes. Colors represent Pearson correlation coefficients.Statistical significance is indicated as $*p < 0.05$ and $**p < 0.01$. (B) Volcano plot of differentially expressed genes. Pink indicates upregulated genes, blue indicates downregulated genes, and black indicates genes without significant differential expression. A total of 1159 differentially expressed genes were identified, including 743 upregulated genes and 416 downregulated genes. (C) Heatmap of differentially expressed genes. Red indicates relatively high expression and blue indicates relatively low expression. The full list of differentially expressed genes is provided in **Supplementary Table 1**.

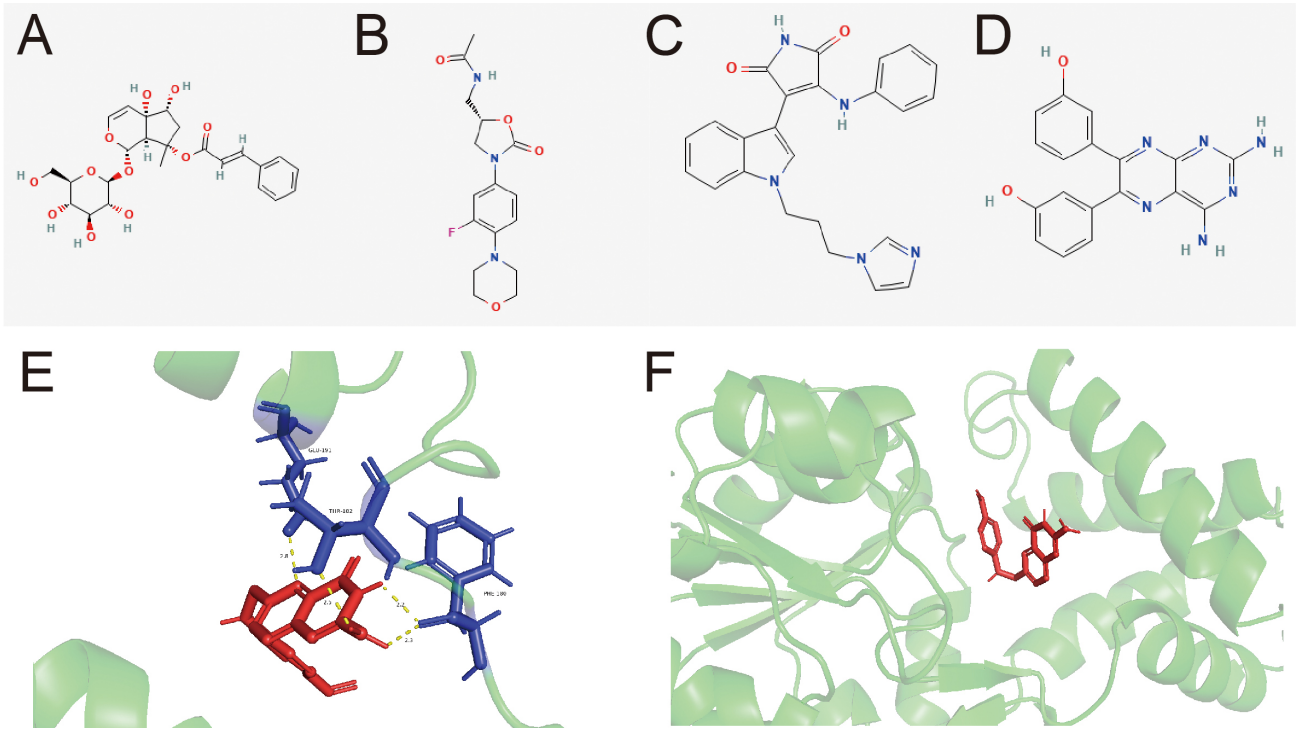

Fig. 9. Chemical structures of the candidate compounds and the key gene–molecule interaction network. (A–D) Two-dimensional (2D) structures of linezolid, harpagoside, TG100-115, and a PKCβ inhibitor. (E,F) Interaction network between key genes and candidate molecules. Each node represents a molecule, and edges indicate molecular docking-derived interactions/associations between molecules. PKCβ, protein kinase C beta.

(Fig. 10D–I; $p < 0.001$). Compared with the 2W group, the 4W group showed significantly increased BV/TV ($p < 0.001$), Tb.N ($p < 0.01$), BMD ($p < 0.01$), and TMD ($p < 0.01$), together with significantly decreased Tb.Sp ($p < 0.001$). Overall, these results suggest partial recovery of trabecular microarchitecture in the 4W group.

Immunohistochemical staining showed that the percentages of L-lactyl lysine-positive and HDHD3-positive cells were significantly increased in the 2W group compared with the control group ($p < 0.001$) and significantly decreased in the 4W group compared with the 2W group ($p < 0.01$) (Fig. 11A–D). RT-qPCR further showed that HDHD3, AHNAK, HMG20B, and IL-1β were significantly upregulated in the 2W group, whereas ARID3B was significantly downregulated ($p < 0.001$). Compared with the 2W group, these changes were partially reversed in the 4W group (Fig. 11E–I). Overall, these findings are generally consistent with the bioinformatics predictions.

Discussion

TMJ OA is a disease with complex aetiology, involving a variety of genetic and epigenetic factors [20]. In this study, GWAS data were integrated with three layers of QTL resources for the first time to systematically explore potential targets for TMJ OA from three biological perspectives: DNA methylation, gene transcript abundance and protein abundance using Mendelian randomization and co-mapping analysis. We found multi-genomic evidence that HMG20B and HDHD3 genes are involved in the development of TMJ OA.

HMG20B is a high mobility group protein mainly located in the nucleus. As a nuclear protein, HMG20B interacts with DNA and other proteins to regulate the activity of transcription factors and participate in cell cycle progression and proliferation regulation [21]. A study has shown that HMG20A interacts with a variety of chromatin modification complexes, localized to the promoter and enhancer regions, and deletion of HMG20A results in changes in chromatin accessibility and dysregulation of specific transcriptional programs, which are key regulators of transcriptional programs during stem cell differentiation into neural crest cells and cardiomyocytes [22]. Deletion of HMG20B also delays the completion of mitotic cell division, triggering abnormalities in this process. Most of HMG20B deficient cells with cytokinesis defects can initiate groove formation and invagination, but complete cell division delay and often fail to separate. In triple negative breast cancer, HMG20B has been reported to interact with the tumor suppressor protein BRCA2 and regulate cell division during cytokinesis [23].

HDHD3 is a mitochondrial hydrolase [24]. Previous animal experiments have shown that up-regulation of HDHD3 expression can maintain the integrity of mitochon-

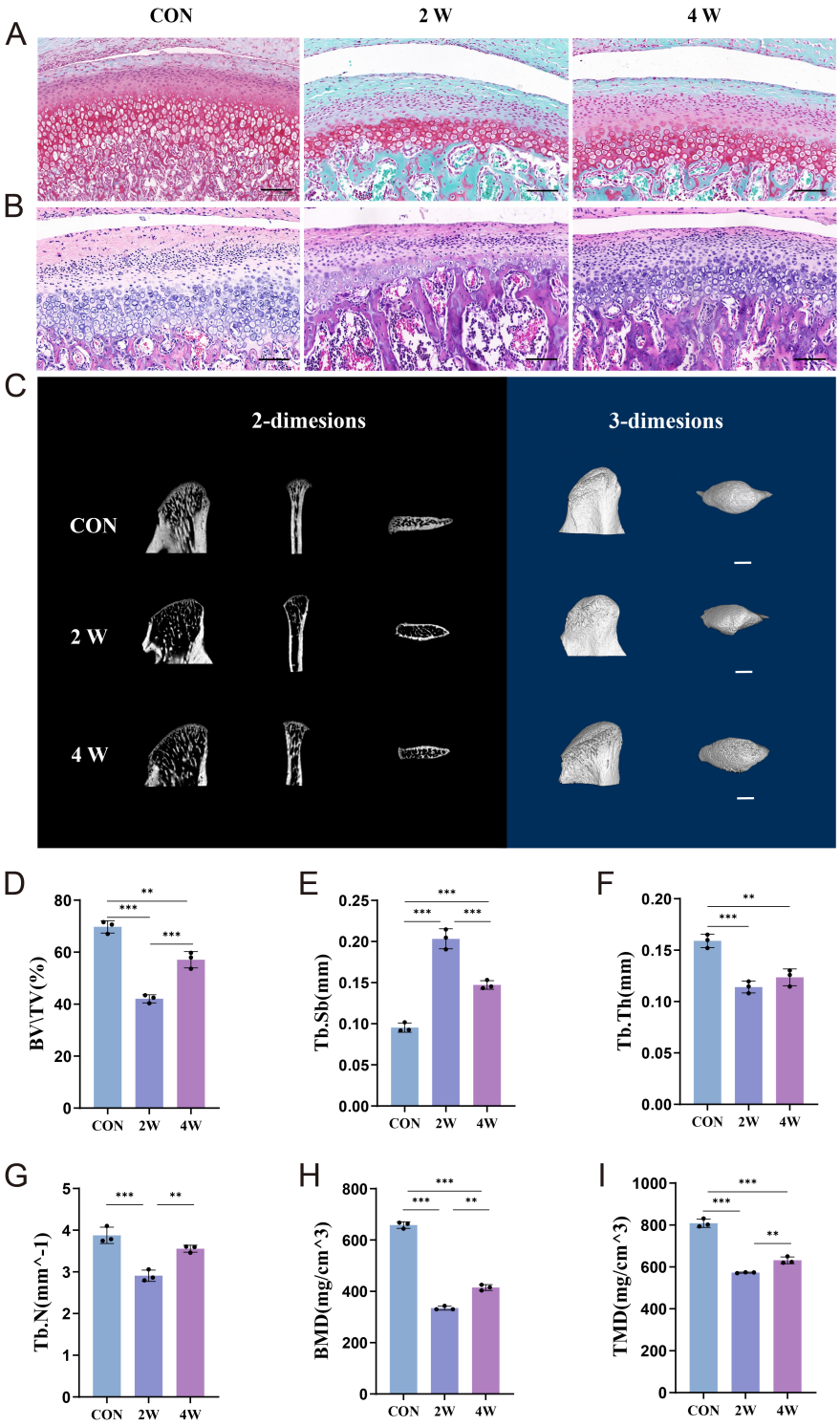

Fig. 10. Morphological analysis of cartilage and bone tissue. (A) Safranin O-fast green staining for the cartilage tissue of rat. Scale bars = 100 µm. (B) H&E staining for the cartilage tissue of rat. Scale bars = 100 µm. (C) Micro-CT images. Scale bars = 1 mm. (D) Bone volume fraction (BV/TV). (E) Trabecular separation (Tb.Sp). (F) Trabecular thickness (Tb.Th). (G) trabecular number (Tb.N). (H) Bone Mineral Density (BMD). (I) Tissue mineral density (TMD). ** indicates $p < 0.01$; *** indicates $p < 0.001$. CT, computed tomography; H&E, hematoxylin and eosin.

dria in mouse hepatocytes, which is closely related to energy homeostasis. Under pathological conditions, HDHD3 was significantly upregulated in peripheral blood of patients with nonalcoholic fatty liver disease (NAFLD) and in mouse liver models [24]. Furthermore, through screening by machine learning algorithms (SVM-RFE/LASSO/RF),

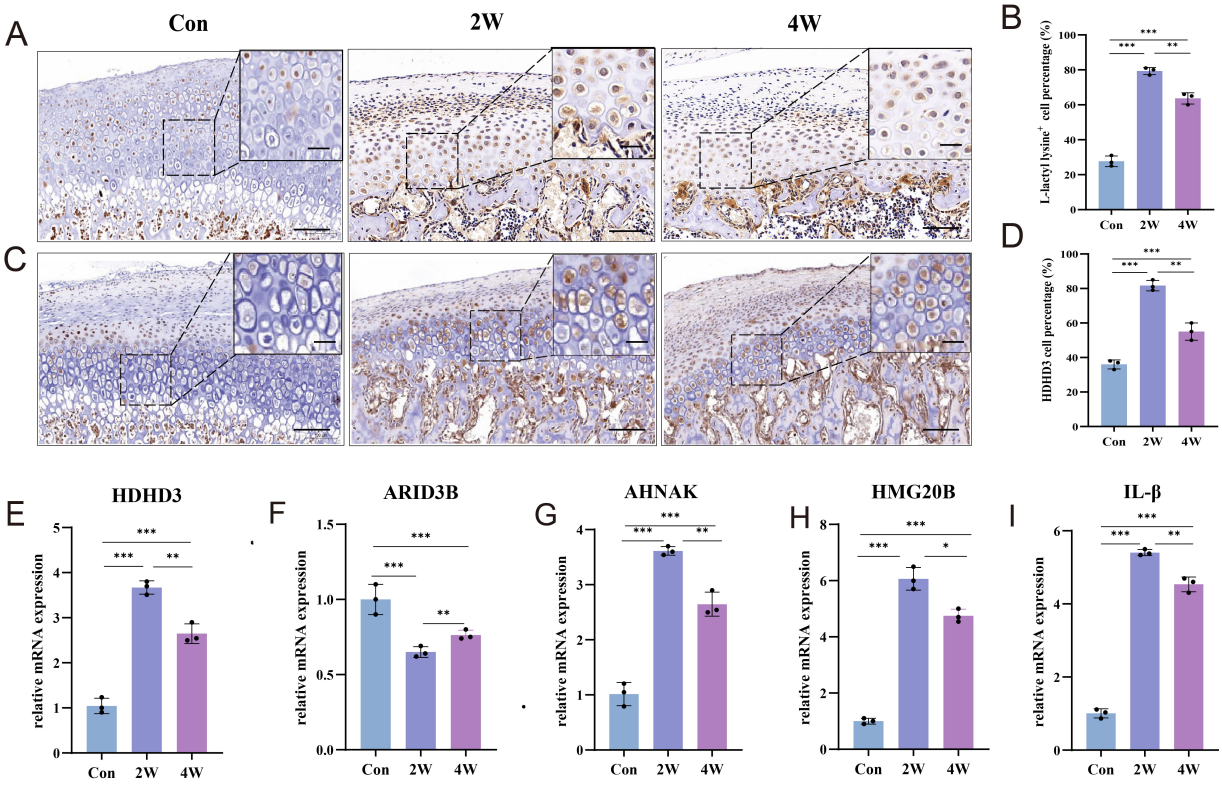

Fig. 11. Immunohistochemistry and RT-qPCR analyses. (A) Representative immunohistochemical (IHC) staining of L-lactyl-lysine in tissues from the control (Con), 2-week (2W), and 4-week (4W) groups. (B) Quantification of the percentage of L-lactyl-lysine–positive cells. (C) Representative IHC staining of HDHD3 in Con, 2W, and 4W tissues. (D) Quantification of the percentage of HDHD3-positive cells. (E–I) Tissue RT-qPCR showing relative mRNA levels of HDHD3, ARID3B, AHNAK, HMG20B, and IL-1β. Scale bar = 100 µm in the main image; scale bar = 15 µm in the inset, *$p < 0.05$, **$p < 0.01$, ***$p < 0.001$.

HDHD3 was identified as a core biomarker for NAFLD diagnosis (AUC = 0.964) and listed as a high-risk factor in the diagnostic nomogram. HDHD3 also showed tubulo-specific high expression in streptozotocin-induced α-2u globulin nephropathy models [25].

Subsequently, we delved into the specific signaling pathways associated with these key genes to elucidate the fundamental molecular mechanisms through which they impact disease progression. Our GSVA revealed enrichment of HDHD3 in glycolysis signaling pathways. It is well-documented that glycolysis plays a pivotal role in osteoarthritis pathogenesis. Within the microenvironment and inflammatory milieu of osteoarthritis, chondrocytes undergo a metabolic shift from oxidative phosphorylation to aerobic glycolysis [26,27]. Heightened glycolytic activity triggers pathological alterations in cartilage structure, including chondrocyte hypertrophy, apoptosis, and extracellular matrix degradation, thereby driving osteoarthritis progression [28]. Previous investigations have demonstrated elevated glycolytic activity in synovial tissue of osteoarthritis patients [29]. Synovial macrophages have much higher glycolytic activity in both osteoarthritis patients and mice; too much glycolysis can kill chondrocytes and accelerate osteoarthritis progression. Mechanical stimuli can also activate the Piezo1-STAT1 signaling pathway to promote HK2 mediated glycolysis in MSCs, thereby promoting the progression of TMJ OA [30]. On the contrary, inhibition of glycolysis (with 3-BP) decreases bone erosion, cartilage damage, and inflammatory cell infiltration in TMJ OA [31]. IL-1β stimulation causes an increase in the glycolysis level of OA chondrocytes under an inflammatory microenvironment condition, which raises the base and maximum respiration rate, metabolic reprogramming, and lowers mitochondrial function [32]. Many studies have found that during inflammation, pyruvate is preferentially converted into lactate via aerobic glycolysis. This is known as the Warburg effect. This metabolic shift leads to the accumulation of lactate in the cytoplasm, which can alter cellular function and contribute to disease progression [33]. Lactate has been reported to induce PKM2 lactylation at K62 in pro-inflammatory macrophages, suppressing inflammatory metabolic adaptation and promoting a transition toward a reparative phenotype [34]. However, whether glycolysis contributes to the progression of TMJ OA through lactate-mediated mechanisms remains unclear.

These findings are broadly consistent with previous TMJ OA studies showing that abnormal mechanical stress, cartilage/subchondral bone remodeling, and metabolic dys-

regulation are closely involved in disease progression. Lu *et al.* [35] reported that multiple signaling pathways are involved in TMJ OA pathology and that inflammation, abnormal mechanical loading, and genetic abnormalities contribute to TMJ OA development. In addition, recent work has emphasized that the pathological progression of TMJ OA involves not only cartilage degeneration but also subchondral bone remodeling, suggesting that both tissues should be considered together when interpreting disease mechanisms [36]. Previous studies have also shown that glycolytic reprogramming and lactate metabolism contribute to TMJ OA pathophysiology. For example, Li *et al.* [37] demonstrated that inhibition of glycolysis by targeting LDHA facilitated hyaluronan synthase 2 synthesis and hyaluronic acid production in synovial fibroblasts of TMJ OA, supporting the importance of metabolic alterations in disease progression. Mechanical signaling has also been implicated in TMJ OA, as Wu *et al.* [38] showed that Piezo1-mediated mechanotransduction participates in condylar degeneration under abnormal stress conditions. In this context, our study extends the existing literature by providing multi-omics evidence that HDHD3 and HMG20B may represent candidate genes associated with these pathological processes, particularly glycolysis- and lactylation-related alterations in TMJ OA.

Correlation analysis between key genes and lactate-related genes revealed clear associations in their expression levels. HDHD3 had a strong positive correlation with AHNAK ($r = 0.850$), and a notable negative correlation with ARID3B ($r = –0.795$). The remaining two genes, AHNAK and ARID3B, have also been identified in the literature as lactate-related genes. ARID3B is a member of the ARID (AT-rich interaction domain) protein family that functions as a transcriptional regulator involved in gene expression and cell differentiation [39]. It also participates in metabolic reprogramming by altering epigenetic modifications. On the other hand, AHNAK is a large scaffold protein with a molecular weight exceeding 700 kDa and is expressed in various tissues [40]. AHNAK plays important roles in cell membrane repair, signal transduction, and cell adhesion. It is also involved in multiple processes, including calcium channel regulation, cell migration, and inflammatory responses [41].

FMR rat models were established for 2 and 4 weeks. Safranin O/Fast Green staining showed that glycosaminoglycan content was lower in the FMR model group than in the control group, indicating severe TMJ cartilage damage. Micro-CT analysis also revealed obvious subchondral bone resorption in both the 2-week and 4-week FMR groups, suggesting joint destruction in the experimental rats. IHC staining showed increased L-lactyl lysine, indicating that lysine residues were modified through the addition of L-lactyl groups to proteins [42]. Lactate is an important metabolic product *in vivo* and participates in both physiological and pathological processes. The degree of lactylation is associated with intracellular lactate levels [43]. The results showed that, in cartilage tissue from FMR rat models, the mRNA levels of IL-1β, the key genes HMG20B and HDHD3, and the lactate-related gene AHNAK were increased after mechanical compression, whereas ARID3B expression was decreased. These *in vivo* findings are consistent with the previous bioinformatics analyses, suggesting that glycolysis-associated lactate metabolism may contribute to the progression of TMJ OA.

Folic acid was identified as a potential candidate compound for TMJ OA based on drug screening and molecular docking analysis. As a water-soluble vitamin (vitamin B9), folic acid is involved in multiple biological processes, including cell growth and proliferation. However, its potential relevance to TMJ OA remains unclear, and further functional studies are needed to clarify its biological significance in this disease context.

Several limitations of this study should be acknowledged. First, the MR analysis was mainly used for candidate gene screening and prioritization. Under the broad multi-omics screening framework and the relatively loose initial threshold, false-positive findings cannot be fully excluded, although we strengthened the robustness of interpretation through colocalization analysis, reverse MR, transcriptomic support, experimental observations, and sensitivity analyses. Second, the molecular QTL datasets were derived from whole blood, peripheral blood, or plasma, whereas TMJ OA is a highly tissue-specific joint disease. Therefore, these blood-based associations should be interpreted as supportive evidence for candidate gene prioritization rather than direct proof of local regulatory mechanisms. Third, the xCell-based immune infiltration analysis should be considered exploratory because of the small sample size and complex tissue composition of the TMJ OA dataset. In addition, the transcriptomic cohort used for expression validation was limited in size. Finally, although our findings support a potential role of HDHD3 in glycolysis- and lactylation-related alterations, the precise mechanistic relationships still require further functional validation.

Overall, our findings suggest that HMG20B and HDHD3 may serve as candidate genes associated with TMJ OA. In particular, HDHD3 may be involved in glycolysis- and lactylation-related alterations during disease progression. These findings provide supportive evidence for a potential role of HDHD3 in TMJ OA and offer a basis for further functional studies to better clarify the underlying biological mechanisms. In addition, folic acid was identified as a candidate compound through drug prediction and molecular docking, and its potential relevance to TMJ OA warrants further investigation.

Conclusion

Overall, the present study provides integrated multi-omics and experimental evidence that helps prioritize

HDHD3 and HMG20B for future investigation in TMJ OA. In particular, HDHD3 may represent a biologically relevant candidate associated with glycolysis- and lactylation-related alterations. In addition, folic acid was identified as a candidate compound through drug prediction and molecular docking, and its potential relevance warrants further evaluation.

Availability of Data and Materials

The original contributions presented in this study are included in the article/**Supplementary Material**. Further inquiries can be directed to the corresponding author.

Author Contributions

XBL and XYuan conceived and designed the study. XBL supervised the study and drafted the manuscript. XYL, CZL, SYY, XYJ and YYZ contributed to investigation, methodology, and visualization. WKY, JG, and XYJ contributed to formal analysis and visualization. HTW, QZ, and XYan contributed to data curation and data interpretation. XYuan contributed to funding acquisition, project administration, supervision, and interpretation of data. All authors were involved in drafting the manuscript or revising it critically for important intellectual content. All authors read and approved the final manuscript and agreed to be accountable for all aspects of the work.

Ethics Approval and Consent to Participate

All animal experimental procedures were reviewed and approved by the Ethics Committee of Qingdao University (Approval No. 20250209SD3220250330031). All animal experiments were conducted in accordance with the institutional guidelines for the care and use of laboratory animals of Qingdao University and complied with the ARRIVE guidelines 2.0 where applicable.

Acknowledgment

Not applicable.

Funding

This work was supported by grants 32171303 from the National Natural Science Foundation of China.

Conflict of Interest

The authors declare no conflict of interest.

Supplementary Material

Supplementary material associated with this article can be found, in the online version, at https://doi.org/10.24976/Discov.Med.202638209.149.

References

[1] Al-Hadad SA, Chen P, Zhao Y, Li C, Zhang C, Alshoaibi LH, *et al*. Comprehensive Three-Dimensional Evaluation of Temporomandibular Joint Changes Following Stabilization Splint Therapy. International Dental Journal. 2025; 75: 100845. https://doi.org/10.1016/j.identj.2025.100845.

[2] Xiang Y, Song J, Liang Y, Sun J, Zheng Z. Causal relationship between psychiatric traits and temporomandibular disorders: a bidirectional two-sample Mendelian randomization study. Clinical Oral Investigations. 2023; 27: 7513–7521. https://doi.org/10.1007/s00784-023-05339-x.

[3] Song H, Lee JY, Huh KH, Park JW. Long-term Changes of Temporomandibular Joint Osteoarthritis on Computed Tomography. Scientific Reports. 2020; 10: 6731. https://doi.org/10.1038/s41598-020-63493-8.

[4] Tao Y, Hua G, Min S, Xiao-Hong L, Jia-Hui J, Biao T, *et al*. Verification of biological markers of subacute cutaneous lupus erythematosus via TMT labelling proteomics combined with transcriptome data. Annals of Medicine. 2025; 57: 2500696. https://doi.org/10.1080/07853890.2025.2500696.

[5] Sun BB, Chiou J, Traylor M, Benner C, Hsu YH, Richardson TG, *et al*. Plasma proteomic associations with genetics and health in the UK Biobank. Nature. 2023; 622: 329–338. https://doi.org/10.1038/s41586-023-06592-6.

[6] Tao T, Mo X, Zhao L. Identifying novel potential drug targets for endometriosis via plasma proteome screening. Frontiers in Endocrinology. 2024; 15: 1416978. https://doi.org/10.3389/fendo.2024.1416978.

[7] Zheng J, Haberland V, Baird D, Walker V, Haycock PC, Hurle MR, *et al*. Phenome-wide Mendelian randomization mapping the influence of the plasma proteome on complex diseases. Nature Genetics. 2020; 52: 1122–1131. https://doi.org/10.1038/s41588-020-0682-6.

[8] Ken-Dror G, Humphries SE, Kumari M, Kivimaki M, Drenos F. A genetic instrument for Mendelian randomization of fibrinogen. European Journal of Epidemiology. 2012; 27: 267–279. https://doi.org/10.1007/s10654-012-9666-x.

[9] Wang G, Mao W, Zhang Y, Yang H, Zhu M, Li Y, *et al*. Multi-omics and Systematic Analyses Reveal the Roles of Hemoglobin and the HIF-1 Pathway in Polycystic Ovary Syndrome. Advanced Science (Weinheim, Baden-Wurttemberg, Germany). 2025; 12: e2411679. https://doi.org/10.1002/advs.202411679.

[10] Skrivankova VW, Richmond RC, Woolf BAR, Yarmolinsky J, Davies NM, Swanson SA, *et al*. Strengthening the Reporting of Observational Studies in Epidemiology Using Mendelian Randomization: The STROBE-MR Statement. JAMA. 2021; 326: 1614–1621. https://doi.org/10.1001/jama.2021.18236.

[11] Ma H, Chen Y. Examining the causal relationship between sex hormone-binding globulin (SHBG) and infertility: A Mendelian randomization study. PloS One. 2024; 19: e0304216. https://doi.org/10.1371/journal.pone.0304216.

[12] Guo J, Si G, Song X, Si F. Association of B cells and the risk of Esophageal cancer: a bidirectional two-sample mendelian randomization study. BMC Cancer. 2024; 24: 1416. https://doi.org/10.1186/s12885-024-13166-w.

[13] Gao J, Bi X, Jiang W, Wang Y. Integration of multi-omics quantitative trait loci evidence reveals novel susceptibility genes for Alzheimer's disease. Scientific Reports. 2025; 15: 30158. https://doi.org/10.1038/s41598-025-12290-2.

[14] Hatton AA, Cheng FF, Lin T, Shen RJ, Chen J, Zheng Z, *et al*. Genetic control of DNA methylation is largely shared across European and East Asian populations. Nature Communications. 2024; 15: 2713. https://doi.org/10.1038/s41467-024-47005-0.

[15] Ferkingstad E, Sulem P, Atlason BA, Sveinbjornsson G, Magnusson MI, Styrmisdottir EL, *et al*. Large-scale integration of the plasma proteome with genetics and disease. Na-

ture Genetics. 2021; 53: 1712–1721. https://doi.org/10.1038/s41588-021-00978-w.

[16] Xiao Y, Yue Z, Zijing H, Yao Z, Sui M, Xuemin Z, *et al*. Mechanical compression induces chondrocyte hypertrophy by regulating Runx2 O-GlcNAcylation during temporomandibular joint condyle degeneration. Bone & Joint Research. 2025; 14: 209–222. https://doi.org/10.1302/2046-3758.143.BJR-2024-0257.R1.

[17] Cheng Z, Huang H, Li M, Liang X, Tan Y, Chen Y. Lactylation-Related Gene Signature Effectively Predicts Prognosis and Treatment Responsiveness in Hepatocellular Carcinoma. Pharmaceuticals (Basel, Switzerland). 2023; 16: 644. https://doi.org/10.3390/ph16050644.

[18] Yadalam PK, Sivasankari T, Rengaraj S, Mugri MH, Sayed M, Khan SS, *et al*. Gene Interaction Network Analysis Reveals IFI44L as a Drug Target in Rheumatoid Arthritis and Periodontitis. Molecules (Basel, Switzerland). 2022; 27: 2749. https://doi.org/10.3390/molecules27092749.

[19] Zheng Y, Ji S, Li X, Feng Q. Active ingredients and molecular targets of *Taraxacum mongolicum* against hepatocellular carcinoma: network pharmacology, molecular docking, and molecular dynamics simulation analysis. PeerJ. 2022; 10: e13737. https://doi.org/10.7717/peerj.13737.

[20] Wen S, Santander J, Barria D, Salazar LA, Sandoval C, Arias C, *et al*. Epigenetic Biomarkers in Temporomandibular Joint Osteoarthritis: An Emerging Target in Treatment. International Journal of Molecular Sciences. 2025; 26: 3668. https://doi.org/10.3390/ijms26083668.

[21] Lee M, Daniels MJ, Garnett MJ, Venkitaraman AR. A mitotic function for the high-mobility group protein HMG20b regulated by its interaction with the BRC repeats of the BRCA2 tumor suppressor. Oncogene. 2011; 30: 3360–3369. https://doi.org/10.1038/onc.2011.55.

[22] Herchenröther A, Gossen S, Friedrich T, Reim A, Daus N, Diegmüller F, *et al*. The H2A.Z and NuRD associated protein HMG20A controls early head and heart developmental transcription programs. Nature Communications. 2023; 14: 472. https://doi.org/10.1038/s41467-023-36114-x.

[23] Lee M, Venkitaraman AR. A cancer-associated mutation inactivates a region of the high-mobility group protein HMG20b essential for cytokinesis. Cell Cycle (Georgetown, Tex.). 2014; 13: 2554–2563. https://doi.org/10.4161/15384101.2014.942204.

[24] Wang B, Yu H, Gao J, Yang L, Zhang Y, Yuan X, *et al*. Machine learning deciphers the significance of mitochondrial regulators on the diagnosis and subtype classification in non-alcoholic fatty liver disease. Heliyon. 2024; 10: e29860. https://doi.org/10.1016/j.heliyon.2024.e29860.

[25] Kengkoom K, Angkhasirisap W, Kanjanapruthipong T, Tungtrakanpoung R, Tuentam K, Phansom N, *et al*. Streptozotocin induces alpha-2u globulin nephropathy in male rats during diabetic kidney disease. BMC Veterinary Research. 2021; 17: 105. https://doi.org/10.1186/s12917-021-02814-z.

[26] Gong Z, Zhu J, Chen J, Feng F, Zhang H, Zhang Z, *et al*. CircRREB1 mediates lipid metabolism related senescent phenotypes in chondrocytes through FASN post-translational modifications. Nature Communications. 2023; 14: 5242. https://doi.org/10.1038/s41467-023-40975-7.

[27] Cao X, Yang X, Zhang P, Xu J, Zhao J, Yang E. Targeting Txnip-mediated metabolic reprogramming has therapeutic potential for osteoarthritis. Cell Death Discovery. 2025; 11: 110. https://doi.org/10.1038/s41420-025-02394-z.

[28] Veronesi F, Costa V, Bellavia D, Basoli V, Giavaresi G. Epigenetic Modifications of MiRNAs in Osteoarthritis: A Systematic Review on Their Methylation Levels and Effects on Chondrocytes, Extracellular Matrix and Joint Inflammation. Cells. 2023; 12: 1821. https://doi.org/10.3390/cells12141821.

[29] Xu D, Liang J, Lin J, Yu C. PKM2: A Potential Regulator of Rheumatoid Arthritis via Glycolytic and Non-Glycolytic Pathways. Frontiers in Immunology. 2019; 10: 2919. https://doi.org/10.3389/fimmu.2019.02919.

[30] Deng Y, Hou M, Wu Y, Liu Y, Xia X, Yu C, *et al*. SIRT3-PINK1-PKM2 axis prevents osteoarthritis via mitochondrial renewal and metabolic switch. Bone Research. 2025; 13: 36. https://doi.org/10.1038/s41413-025-00413-4.

[31] Zhou Y, Li M, Lin S, Zhu Z, Zhuang Z, Cui S, *et al*. Mechanical sensing protein PIEZO1 controls osteoarthritis via glycolysis mediated mesenchymal stem cells-Th17 cells crosstalk. Cell Death & Disease. 2025; 16: 231. https://doi.org/10.1038/s41419-025-07577-1.

[32] Defois A, Bon N, Charpentier A, Georget M, Gaigeard N, Blanchard F, et al. Osteoarthritic chondrocytes undergo a glycolysis-related metabolic switch upon exposure to IL-1β or TNF. Cell Communication and Signaling. 2023; 21: 137. https://doi.org/10.1186/s12964-023-01150-z

[33] Niu Y, Wang N, Qiao L, Huang Z, Jing G, Fu S, *et al*. Targeting CD4+ T Cell Glucose Metabolism: A Novel Immunotherapeutic Approach for Type 1 Diabetes. Biomolecules. 2025; 15: 770. https://doi.org/10.3390/biom15060770.

[34] Wang J, Yang P, Yu T, Gao M, Liu D, Zhang J, *et al*. Lactylation of PKM2 suppresses inflammatory metabolic adaptation in pro-inflammatory macrophages. International Journal of Biological Sciences. 2022; 18: 6210–6225. https://doi.org/10.7150/ijbs.75434.

[35] Lu K, Ma F, Yi D, Yu H, Tong L, Chen D. Molecular signaling in temporomandibular joint osteoarthritis. Journal of Orthopaedic Translation. 2021; 32: 21–27. https://doi.org/10.1016/j.jot.2021.07.001.

[36] Cardoneanu A, Macovei LA, Burlui AM, Mihai IR, Bratoiu I, Rezus II, *et al*. Temporomandibular Joint Osteoarthritis: Pathogenic Mechanisms Involving the Cartilage and Subchondral Bone, and Potential Therapeutic Strategies for Joint Regeneration. International Journal of Molecular Sciences. 2022; 24: 171. https://doi.org/10.3390/ijms24010171.

[37] Li HM, Guo HL, Xu C, Liu L, Hu SY, Hu ZH, *et al*. Inhibition of glycolysis by targeting lactate dehydrogenase A facilitates hyaluronan synthase 2 synthesis in synovial fibroblasts of temporomandibular joint osteoarthritis. Bone. 2020; 141: 115584. https://doi.org/10.1016/j.bone.2020.115584.

[38] Wu CB, Ma T, Ma L, Wang Q, Zhou Q. Piezo1 Affects Temporomandibular Joint Osteoarthritis by Influencing pSmad3. Frontiers in Physiology. 2022; 13: 892089. https://doi.org/10.3389/fphys.2022.892089.

[39] Oguz Erdogan AS, Ozdemirler N, Oyken M, Alper M, Erson-Bensan AE. ARID3B expression in primary breast cancers and breast cancer-derived cell lines. Cellular Oncology (Dordrecht, Netherlands). 2014; 37: 289–296. https://doi.org/10.1007/s13402-014-0185-5.

[40] Marcozzi S, Ciccosanti F, Fimia GM, Piacentini M, Caggiano C, Sette C, *et al*. Analysis of Secreted Proteins from Prepubertal Ovarian Tissues Exposed In Vitro to Cisplatin and LH. Cells. 2022; 11: 1208. https://doi.org/10.3390/cells11071208.

[41] Sundararaj S, Ravindran A, Casarotto MG. AHNAK: The quiet giant in calcium homeostasis. Cell Calcium. 2021; 96: 102403. https://doi.org/10.1016/j.ceca.2021.102403.

[42] Zhang D, Tang Z, Huang H, Zhou G, Cui C, Weng Y, *et al*. Metabolic regulation of gene expression by histone lactylation. Nature. 2019; 574: 575–580. https://doi.org/10.1038/s41586-019-1678-1.

[43] Ren H, Tang Y, Zhang D. The emerging role of protein L-lactylation in metabolic regulation and cell signalling. Nature Metabolism. 2025; 7: 647–664. https://doi.org/10.1038/s42255-025-01259-0.